iScience

CellPress

Article

Orthorhombic Nb_2O_{5-x} for Durable High-Rate Anode of Li-Ion Batteries

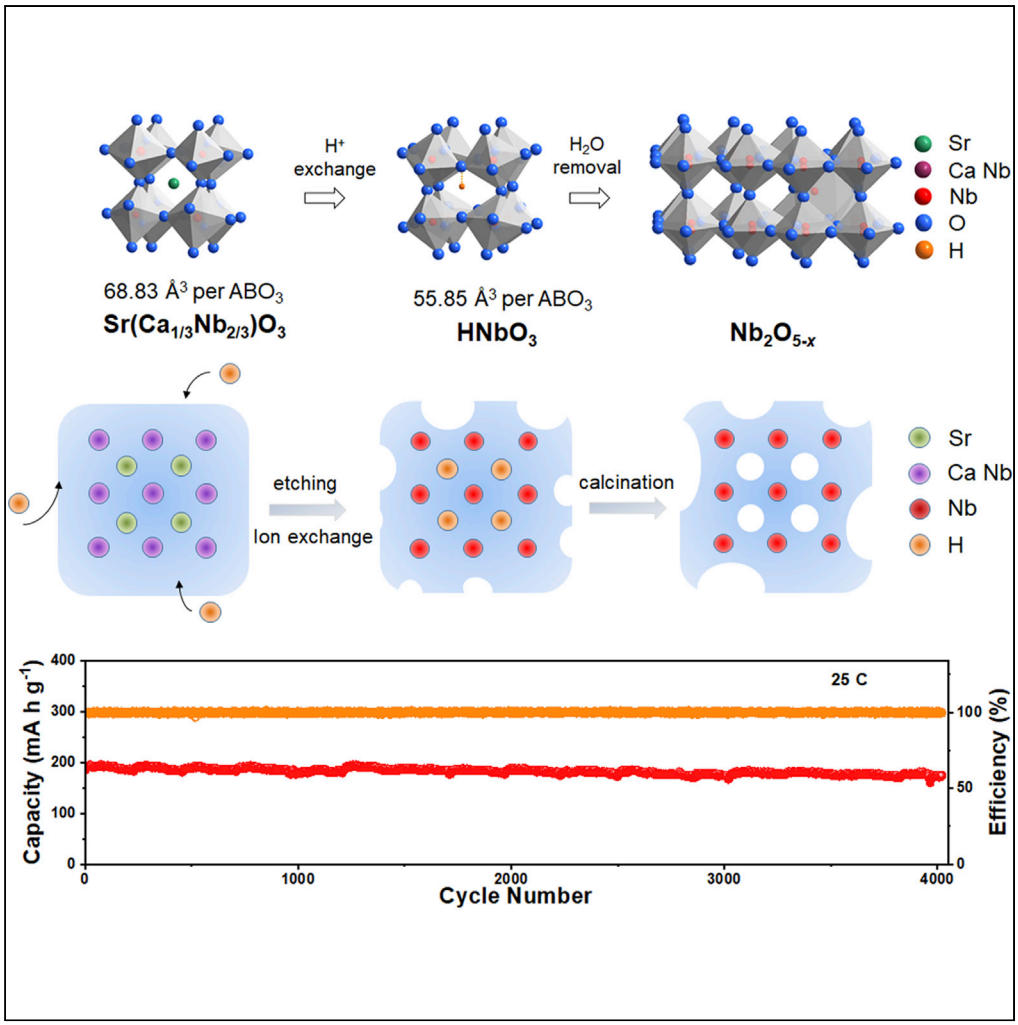

Zichao Liu, Wujie Dong, Jianbo Wang, Chenlong Dong, Yue Lin, I-Wei Chen, Fuqiang Huang

iweichen@seas.upenn.edu (I.-W.C.)
huangfq@pku.edu.cn (F.H.)

HIGHLIGHTS

A novel micro-etching strategy is developed to prepare porous nano-crystal Nb_2O_5

The obtained Nb_2O_5 remains the morphology of the precursor but reconstructs unit cell

Oxygen vacancies and Nb^{4+}/Nb^{5+} are introduced to porous Nb_2O_{5-x} by anoxic annealing

Defect-rich and porous Nb_2O_{5-x} works as durable, high-rate, and safe anode of LIBs

Liu et al., iScience 23, 100767 January 24, 2020
https://doi.org/10.1016/j.isci.2019.100767

iScience

CellPress

Article

Orthorhombic Nb_2O_{5-x} for Durable High-Rate Anode of Li-Ion Batteries

Zichao Liu,[1,5] Wujie Dong,[2,5] Jianbo Wang,[1] Chenlong Dong,[1] Yue Lin,[3] I-Wei Chen,[4,*] and Fuqiang Huang[1,2,6,*]

SUMMARY

$Li_4Ti_5O_{12}$ anode can operate at extraordinarily high rates and for a very long time, but it suffers from a relatively low capacity. This has motivated much research on Nb_2O_5 as an alternative. In this work, we present a scalable chemical processing strategy that maintains the size and morphology of nano-crystal precursor but systematically reconstitutes the unit cell composition, to build defect-rich porous orthorhombic Nb_2O_{5-x} with a high-rate capacity many times those of commercial anodes. The procedure includes etching, proton ion exchange, calcination, and reduction, and the resulting Nb_2O_{5-x} has a capacity of 253 mA h g^{-1} at 0.5C, 187 mA h g^{-1} at 25C, and 130 mA h g^{-1} at 100C, with 93.3% of the 25C capacity remaining after cycling for 4,000 times. These values are much higher than those reported for Nb_2O_5 and $Li_4Ti_5O_{12}$, thanks to more available surface/sub-surface reaction sites and significantly improved fast ion and electron conductivity.

INTRODUCTION

Commercial lithium-ion $Li_4Ti_5O_{12}$ anodes currently in use in power lithium ion batteries (LIBs) on buses have an advantage over other commercial anodes because their capacity can sustain high rates. For example, graphite has a capacity of 62 mA h g^{-1} at 10 C compared with 311 mA h g^{-1} at 0.5 C and silicon-carbon composite (Si/C) has 54 mA h g^{-1} at 10 C and 440 mA h g^{-1} at 0.5 C, but $Li_4Ti_5O_{12}$'s capacity of 145 mA h g^{-1} at 10 C is rather close to that of 170 mA h g^{-1} at 0.5 C (Wang et al., 2015). Nevertheless, the capacity of $Li_4Ti_5O_{12}$ is relatively low, so there is much impetus to find a higher-capacity replacement that can retain the advantage of rate insensitivity.

As $Li_4Ti_5O_{12}$, other early transition metal oxides comprised of similar mostly corner-sharing octahedra can also reversibly incorporate Li while retaining the structure without inordinate volume changes, thus providing better rate and cyclic performance. Among them, recent interest has been directed to $Nb_xW_yO_z$ (Griffith et al., 2018) featuring outstanding anode properties, but being one of the simplest such oxides, Nb_2O_5 has already received much attention. Dunn et al. reported a mesoporous orthorhombic Nb_2O_5 nanocrystal, which, when combined with an equal mass of conducting carbon black, can make electrodes of 145 mA h g^{-1} at 1 C and 105 mA h g^{-1} at 100 C (Augustyn et al., 2013); however, at a more common ratio of active material (Nb_2O_5) to carbon black of ~8:1, its high-rate capacity is still limited. Other studies of orthorhombic Nb_2O_5 (also denoted as T- Nb_2O_5 in the literature) in the form of hollow nanosphere (Kong et al., 2014), nanobelt (Wei et al., 2008), nanosheet (Kong et al., 2015), and nanofiber (Viet et al., 2010) all reported broadly similar properties, with values such as 250 mA h g^{-1} at 0.5 C in the first cycle that drops to 180 mA h g^{-1} in the 50th cycle. Instead of using carbon black, various constructs to introduce current collectors, such as carbonaceous coating or inclusions, co-assemblies of Nb_2O_5 nanorods and carbon fiber (Deng et al., 2018a), and composites with holey graphene, have been explored, which achieved first-cycle values such as 190 mA h g^{-1} at 200 mA g^{-1} (1 C) and 90 mA h g^{-1} at 20,000 mA g^{-1} (100 C) (Sun et al., 2017). These devices already have properties approaching the theoretical capacity (200 mA h g^{-1}) of Nb_2O_5, but they also require complicated designs or synthesis, which is a potentially serious impediment toward practical applications.

Because orthorhombic Nb_2O_5 does have a higher theoretical capacity, we have sought to find a simple fabrication strategy to directly impart fast Li and electron conductivities into additive-free Nb_2O_5 to achieve high performance. Such a strategy is reported in this study, in which we fabricated well-crystallized but highly active defect-rich orthorhombic Nb_2O_5 by robust yet selective acid etching of a parent oxide followed by annealing. When the product is mixed with a modest, standard amount of carbon black and conducting binder, the resulting anode outperforms all the previously reported Nb_2O_5-based ones, having 253 mA h g^{-1}at 100 mA g^{-1} (0.5 C) and 130 mA h g^{-1} at 20,000 mA g^{-1} (100 C, taking less than 36 s to charge

[1]State Key Laboratory of Rare Earth Materials Chemistry and Applications, College of Chemistry and Molecular Engineering, Peking University, Beijing 100871, P. R. China

[2]State Key Laboratory of High Performance Ceramics and Superfine Microstructures, Shanghai Institute of Ceramics, Chinese Academy of Sciences, Shanghai 200050, P. R. China

[3]Hefei National Laboratory for Physical Sciences at the Microscale, University of Science and Technology of China, Hefei, Anhui 230026, P. R. China

[4]Department of Materials Science and Engineering, University of Pennsylvania, Philadelphia, PA 19104, USA

[5]These authors contributed equally

[6]Lead Contact

*Correspondence: iweichen@seas.upenn.edu (I.-W.C.), huangfq@pku.edu.cn (F.H.)

https://doi.org/10.1016/j.isci.2019.100767

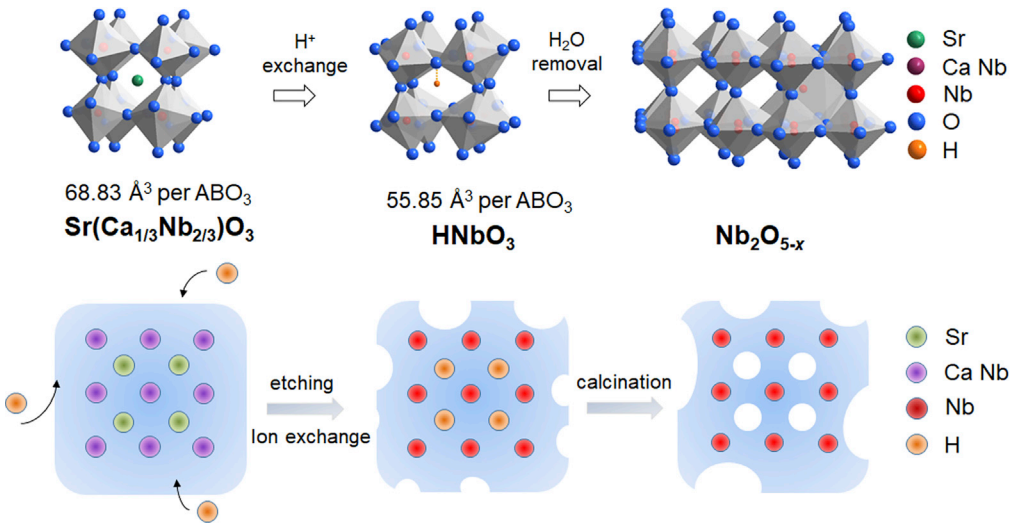

Figure 1. Synthesis Schematic

Structure: chemical evolution toward Nb_2O_{5-x}.

or discharge). With a reasonable tap density of 1.3 g cm^{-3}, its cyclic performance is especially outstanding, having a stable capacity, e.g., 176 mA h g^{-1} at 25 C (5,000 mA g^{-1}), over 4,000 cycles. Therefore, our Nb_2O_5 could be a very attractive alternative to commercial high-rate $Li_4Ti_5O_{12}$ anode (170 mA h g^{-1} at 0.5 C, 130 mA h g^{-1} at 20 C, 80 mA h g^{-1} at 80 C) (Wang et al., 2015) as a durable high-rate power source in practical applications.

RESULTS

Synthesis and Physicochemical Property

The precursor $Sr(Ca_{1/3}Nb_{2/3})O_3$ is an ABO_3 perovskite that also comprises a network of corner-sharing BO_6 octahedra. It was chosen because Sr and Ca, being more basic than Nb, can be easily etched away in acid to remove all the *A*-site Sr and *B*-site Ca, hopefully leaving behind an intact yet atomically loose/open framework (Figure 1). Acid etching, however, introduced H into the framework by ion exchange, forming $HNbO_3$ (Figure 1), but H can be driven away later by calcination. The diffraction peaks (Figure 2A) of our $Sr(Ca_{1/3}Nb_{2/3})O_3$ match well with those of disordered $Sr(Ca_{1/3}Nb_{2/3})O_3$ (JCPDS 17-0174), but they are slightly shifted toward higher angles indicating a 1.73% smaller unit cell (202.16 $Å^3$ *vs.* 205.73 $Å^3$). The diffraction peaks of $HNbO_3$ also find good correspondence with those of perovskite $HNbO_3$ (JCPDS 36-0794), but the unit cell is 3.92% larger in our material (465.04 $Å^3$ *vs.* 446.82 $Å^3$). Overall, the per-formula volume shrinks by 18.8% from 68.83 $Å^3$ in $Sr(Ca_{1/3}Nb_{2/3})O_3$ to 55.85 $Å^3$ in $HNbO_3$, which suggests large internal strains left in $HNbO_3$.

We believe one cause of such large internal strains is the reconstitutive nature of the acid-etch/ion-exchange process. Here, by reconstitution, we mean a compositional modification at the level of local atomic structure that is repeated throughout the entire crystal, yet this is accomplished without reconstructing the overall microstructure or the size/shape of the crystal. This is supported by the SEM images showing almost the same size distribution and morphology for $Sr(Ca_{1/3}Nb_{2/3})O_3$ (Figure S1A) and $HNbO_3$ (Figure S1B), indicating reconstitution at the unit cell level does not involve crystallite dissolution/reprecipitation that will most certainly result in a rather different morphology and size. Indeed, when a higher concentration of HCl and a longer reaction time were used, dissolution/reprecipitation did take place, producing larger, hexagonal platelets as shown in Figure S1E.

As $HNbO_3$ is heated, it dehydrates at above 200°C, and such process is mostly complete by 400°C according to TGA (Figure S2A). Annealing at 700°C under Ar gave the final product Nb_2O_{5-x}, which has the same structure as the Nb_2O_5 phase identified by JCPDS 27-1003 (Figure 2A) with nearly the same lattice parameters. Still, its particle size and morphology remain largely similar to those of $Sr(Ca_{1/3}Nb_{2/3})O_3$ and $HNbO_3$ as shown in Figure S1C. Therefore, the entire process is most likely reconstitutive at the unit cell level and

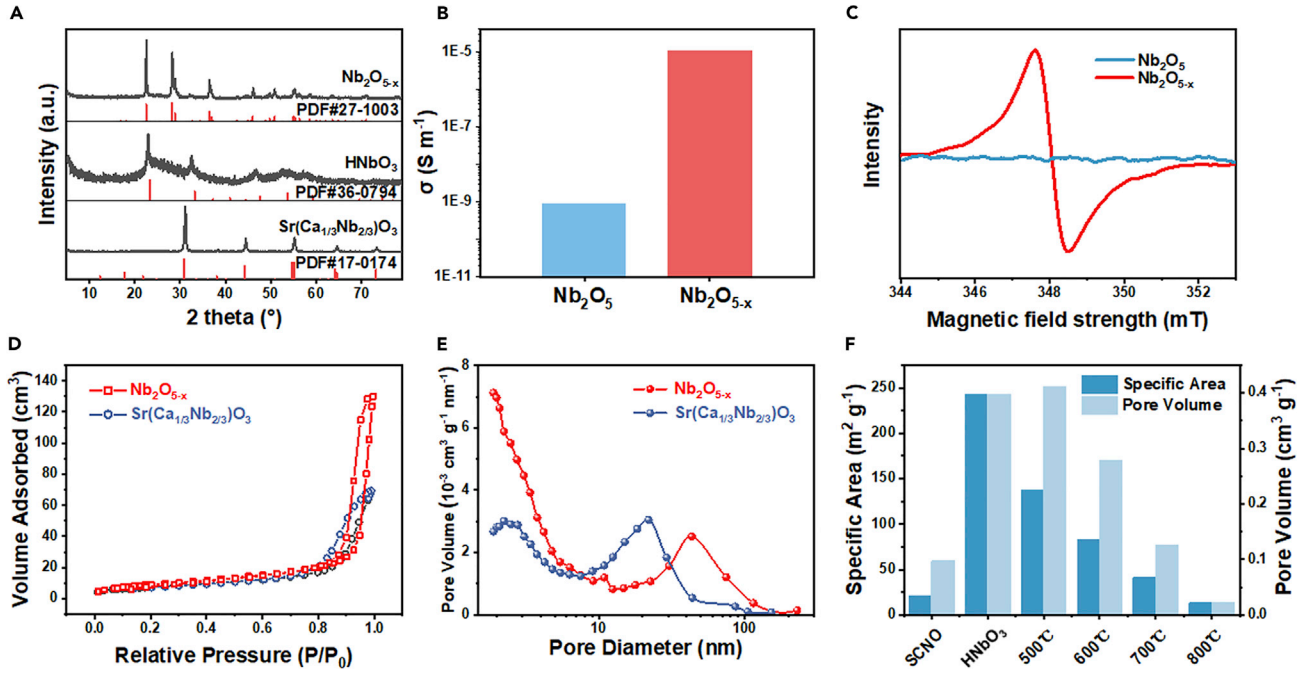

Figure 2. Physical Properties of Nb_2O_{5-x}

(A and B) (A) XRD patterns of $Sr(Ca_{1/3}Nb_{2/3})O_3$, $HNbO_3$, and Nb_2O_{5-x}. There is no indication of superlattice reflection in $Sr(Ca_{1/3}Nb_{2/3})O_3$ due to *B*-site ordering, which if present occurs at about 19°. The lattice parameter of Nb_2O_{5-x} {a = 6.171973 Å, b = 29.287891 Å, and c = 3.931551 Å} are nearly the same as that of JCPDS: 6.168 Å, 29.312 Å and 3.936 Å; see Rietveld refinement result in Figure S3; (B) conductivity of air-annealed Nb_2O_5 and Ar-annealed Nb_2O_{5-x}. (C–E) (C) EPR spectra of Nb_2O_{5-x} and Nb_2O_5; (D) nitrogen adsorption-desorption isotherms; and (E) BJH adsorption pore size distribution analysis of $Sr(Ca_{1/3}Nb_{2/3})O_3$ and Nb_2O_{5-x}.

(F) Specific area and pore volume of $Sr(Ca_{1/3}Nb_{2/3})O_3$ (noted as SCNO); $HNbO_3$; and 500°C-, 600°C-, 700°C-, and 800°C-annealed Nb_2O_{5-x}.

non-destructive at the single crystal level. Lastly, reheating Nb_2O_{5-x} in air to 800°C in TGA causes full oxidation (Figure S2B), from which we determined x = 0.61 although the accuracy of this value is likely to be compromised somewhat because the decomposition of hydroxyl residues may still persist to high temperature.

The Ar-annealed Nb_2O_{5-x} is black (Figures S4A–S4C), and it absorbs more light at longer wavelength outside the UV-absorption edge (Figure S4D UV-vis). Because x = 0.61 indicates the presence of Nb^{4+} or holes, one expects greatly improved conductivity over that of air-annealed Nb_2O_5, which is confirmed (1,000× higher) in Figures 2B and S5. In this respect, black niobia is analogous to black titania that also has greatly improved conductivity and enhanced light absorption compared with fully oxidized white titania (Chen et al., 2011, 2015; Cui et al., 2014; Wang et al., 2013a). Because of surface oxidation, XPS in Figure S6A reveals nearly the same Nb 3*d* spectrum as in white Nb_2O_5 in Figure S6B, with $d_{3/2}$ and $d_{5/2}$ peaks at respective binding energies of 209.8 eV and 207 eV typical for Nb(V)-O bonds in Nb_2O_5. (Near the baseline, the two small peaks at 208.4 eV and 205.6 eV in Figure S6A could be assigned to Nb(IV)-O bonds.) A definitive differentiation between the two oxidation states comes from EPR in Figure 2C, which reveals prominently magnetic Nb in Nb_2O_{5-x} but not in Nb_2O_5. Again, very similar findings were reported for black and white titania: they can be easily distinguished using bulk-sensitive EPR but not surface-limited XPS (Wang et al., 2011, 2013b).

Adsorption-desorption isotherms of N_2 identified distinct loops of type-IV isotherm (IUPAC classification) in all the samples (Figure 2D). A specific surface area of about 41.2 m^2 g^{-1} was found for Nb_2O_{5-x}, twice that (20.8 m^2 g^{-1}) of $Sr(Ca_{1/3}Nb_{2/3})O_3$ (precursor) and three times the value of Nb_2O_5 (14.3 m^2 g^{-1}, Figures S6C and S6D). Compared with $Sr(Ca_{1/3}Nb_{2/3})O_3$, Nb_2O_{5-x} has more pore volume (Figure 2E) especially in the <5 nm region, although it also has pores of 40–50 nm that are larger than the 20 nm pores of $Sr(Ca_{1/3}Nb_{2/3})O_3$. This is not surprising in view of the defects and lattice vacancies created by acid etching. Further specific area and pore volume analysis found the etched product $HNbO_3$ had the largest specific

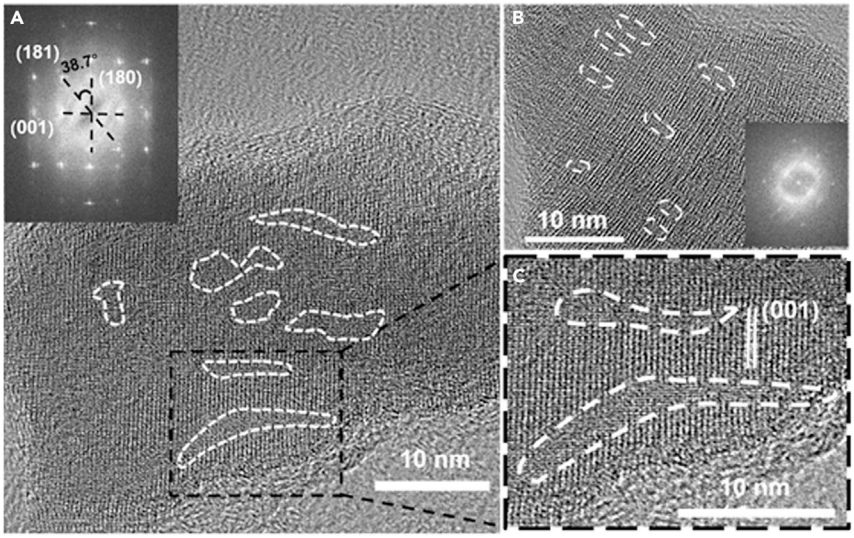

Figure 3. Defect-Rich Nb_2O_{5-x} Crystal

HRTEM images showing coexistence of crystalline structure and extended defects. Insets in (A) and (B) are their fast Fourier transforms; (C) is a partially enlarged image of (A).

surface area (242.5 $m^2\ g^{-1}$) and pore volume (0.3979 $cm^3\ g^{-1}$), which represents a huge increase from those of the $Sr(Ca_{1/3}Nb_{2/3})O_3$ precursor (20.8 $m^2\ g^{-1}$ and 0.0978 $cm^3\ g^{-1}$, respectively.) These values progressively decrease during Ar annealing as shown in Figure 2F, although the pore volume did initially increase at 500°C likely because of dehydration of $HNbO_3$ that occurs below this temperature. Meanwhile, maximum conductivity is reached after ~600–700°C annealing (Figure S5), presumably due to increased hole concentration. So the optimal temperature for electrochemical performance that relies on specific surface area, porosity, and conductivity should lie around 600–700°C as will be seen later in electrochemical testing.

Defect-Rich Porous Crystal

A detailed examination of nanoscale structure and defects was carried out on Nb_2O_{5-x} using TEM. First, we verified that each particle is a single crystal. Next, we have chosen to orient the crystal to be perpendicular to 001 and 180 as shown in Figure 3 because it was reported that Li insertion occurs most easily along these planes (Brezesinski et al., 2010; Kim et al., 2012; Kumagai et al., 1999). (See inset in Figure 3A, which is a fast Fourier transform of the image.) In this single crystal, there is very prominent diffuse scattering around (000) but not at (000), which is a distinct feature of displacement or alloying randomness. In our material, alloying randomness may arise from the random placement of filled and vacant sites, namely atoms and vacancies, on both the Nb and O sublattices. Such diffuse scattering is especially prominent in Figure 3A as indicated by streaking, likely due to displacement waves to accommodate copious vacancies. At the direct, atomic level, although the overall structure is clearly crystalline, there are numerous disordered regions, some arranged into bands of various thickness (many around 2–3 nm), length (varying from 3–20 nm), and orientations, as encircled by white dotted lines in Figures 3A–3C (Xie et al., 2017). (Disorder and nanopores are also obvious in $HNbO_3$ in Figure S7, taken before high-temperature calcination.) This coexistence of order and disorder is especially evident in Figure 3B, and its extensive nature is highlighted in Figure 3C that is an enlarged view of one region in Figure 3A.

These disorders mostly likely originate from the interplay of (1) cation removal, from Sr, to Ca to H; (2) anion removal, from reduction; and (3) large changes in unit cell volume from $Sr(Ca_{1/3}Nb_{2/3})O_3$ to $HNbO_3$ though not to Nb_2O_{5-x}, all the while maintaining the same octahedral framework and the same crystal construct over a length scale of the order of 100 nm, which is the (single crystal) particle size in Figure S1. This implies the creation of a large vacancy population and internal strains, the latter activating the former to collapse (most likely by cooperative shear that is known to be more expedient than diffusion) into vacancy clusters and stacking faults; some of these final, extended, vacancy-derived defects may provide paths for rapid Li transport as speculated in the literature (Come et al., 2014; Griffith et al., 2016; Kim et al., 2012; Kodama

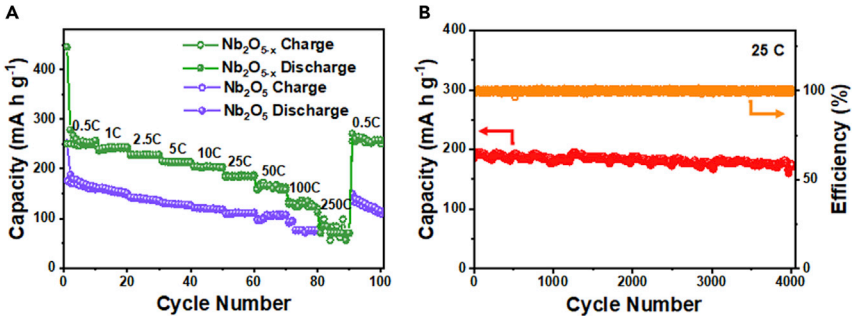

Figure 4. High-Rate Capacity and Stability

(A) Rate performance of Nb_2O_{5-x} and Nb_2O_5, (B) cyclic performance of Nb_2O_{5-x} at a rate of 25 C (5,000 mA g^{-1}).

et al., 2006; Lubimtsev et al., 2013). They may also afford a wider variety of electrochemically active sites to facilitate fast-rate charging/discharging. Lastly, they may more easily accommodate volume changes upon Li insertion/extraction, thus helping to maintain structural integrity during electrochemical cycling.

Electrochemical Property and Performance

With Nb_2O_5 as a reference, the improved performance of Nb_2O_{5-x} is best illustrated using galvanostatic cyclic charge/discharge (CC) tests in Figure 4A for various charging rates. At 0.5 C, Nb_2O_{5-x} has a capacity of 253 mA h g^{-1}, more than 50% higher than that of Nb_2O_5 (160 mA h g^{-1}). This advantage is maintained at other rates, e.g., at 25 C (5,000 mA g^{-1}), Nb_2O_{5-x} has 187 mA h g^{-1} *vs.* 105 mA h g^{-1} for Nb_2O_5. Even at the extremely high rates of 100 C and 250 C, Nb_2O_{5-x} still obtains 130 mA h g^{-1} (*vs.* 75 mA h g^{-1} for Nb_2O_5) and 70 mA h g^{-1} (Nb_2O_5's was too small to measure), respectively. In addition, because of the high cut-off voltage (1–3 V), we also used Al foil as a cheaper substitute for Cu-foil current collector and again obtained a very similar high capacity at high rates as shown in Figure S8. Superior reversibility and stability was also demonstrated by the CC tests, e.g., when the rate returned to 0.5 C at the end of the test, Nb_2O_{5-x} recovered 252 mA h g^{-1}—the same as the initial value—whereas Nb_2O_5's capacity had by now faded to 112 mA h g^{-1} from the initial value of 160 mA h g^{-1}. Outstanding reversibility and durability were further confirmed by extended CC tests at 25 C (Figure 4B): throughout the 4,000-cycle test, 100% coulombic efficiency was achieved, and the final specific capacity was 93.3% of the original. This represents a change of only 0.00167%/cycle, which is remarkable for an extraordinarily large capacity and high rate for this class of electrodes after relatively long cycling. In contrast, when long-term durability was achieved for other electrodes, it was usually with a much more limited capacity or shorter cycles. Examples are carbon/Nb_2O_5 composite at 70–80 mA h g^{-1} (charging/discharging rate not specified in this report) maintaining ~87% after 70,000 cycles (Song et al., 2017), Nb_2O_5@graphene at 70–80 mAh g^{-1} at 50 C maintaining ~70% after 20,000 cycles (Deng et al., 2018b), and urchin-like Nb_2O_5 at 131 mA h g^{-1} at 5 C maintaining 98% after 1,000 cycles (Liu et al., 2016a).

The CV profiles in Figure 5A confirm a larger current density for Nb_2O_{5-x} throughout the entire test range (also see Figure S9 for performance after other Ar-annealing temperatures). Note that its cathodic peaks are broader than Nb_2O_5's, which has two distinct peaks around 1.48 V and 1.79 V. This supports our expectation that copious defect sites in Nb_2O_{5-x} may offer a wider variety of electrochemically active sites for charging/discharging. To provide a more quantitative measure of this aspect, we used the CV test to measure the equivalent specific capacitance C_L from $dQ/dt = C_L dV/dt$, which is expected to hold in the voltage range away from any peak, such as from 2.9 V to 3 V in Figure 5A. As shown in Figure S10B, the CV profiles in this range collected at 3 to 10 mV s^{-1} give a current at 2.95 V that increases linearly with the voltage scan rate (Figure 5B), from which one obtains C_L = 7.82 mF g^{-1} for Nb_2O_{5-x} *vs.* 0.85 mF g^{-1} for Nb_2O_5. Since the geometric surface areas of Nb_2O_{5-x} (41.2 m^2 g^{-1}) and Nb_2O_5 (14.3 m^2 g^{-1}) differ only by a factor of 3, the almost 10× difference in C_L is a testament of more—or more active—electrochemical sites available per unit surface area in Nb_2O_{5-x}. Electrochemical impedance spectroscopy (EIS) using the standard electrode configuration (Figure S11A) and the ion-blocking electrode configuration (Figure S11B) (Kanno and Murayama, 2001) also measured a (mostly electron) charge transfer resistance (R_{ct}) at high frequency, 54.6 Ω for Nb_2O_{5-x} *vs.* 111 Ω for Nb_2O_5, and an ionic conductivity of 2.50×10^{-5} S m^{-1} for Nb_2O_{5-x} *vs.* a value too small to measure for Nb_2O_5. Lastly, the EIS results obtained using the standard electrode configuration

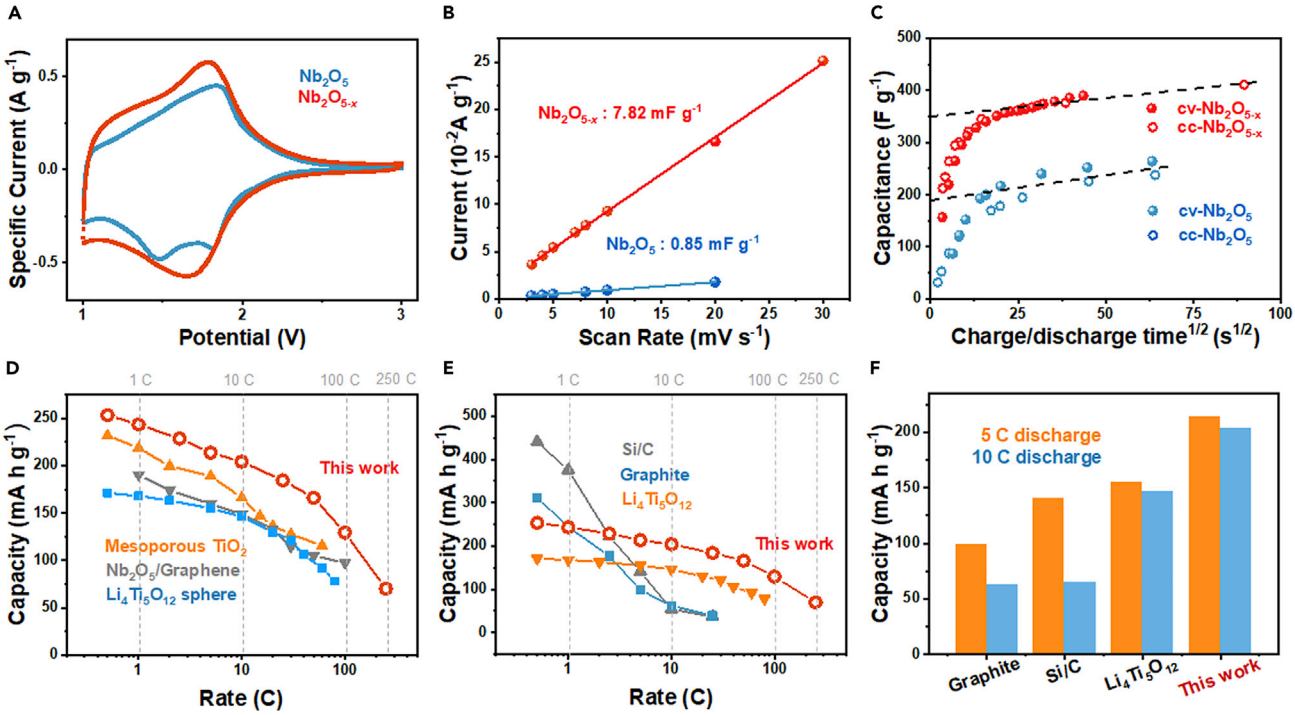

Figure 5. Electrochemical Properties and Performance Comparison

(A) Cyclic voltammetric profiles of Nb_2O_{5-x} and Nb_2O_5.

(B) Current as a function of scan rates for Nb_2O_{5-x} and Nb_2O_5 from CV curves in Figures S10A and S10B.

(C) Capacitance versus square root of half-cycle time in both CV test (solid symbols) from 0.5 to 100 mV s^{-1} and CC test (open symbols) from 0.1 to 20 A g^{-1}. Extrapolated intercept capacitance is rate-independent capacitance k_1, the remainder diffusion-controlled capacitance.

(D) Comparison of rate capacity between this work and three other anode materials reported in the literature (Liu et al., 2011; Sun et al., 2017; Wang et al., 2015).

(E and F) (E) Rate performance comparison between this work and three common commercial anodes, and (F) is their discharge capacities at 5 C and 10 C. ($Li_4Ti_5O_{12}$ reference: Wang et al., 2015)

allowed us to calculate a Li^+ diffusion coefficient, which is 4.836 × 10^{-12} for Nb_2O_{5-x} and 7.547 × 10^{-13} cm^2 s^{-1} for Nb_2O_5. (See Transparent Methods, which follows [Du et al., 2012] and data fitting, shown in Figure S12.) All these results are self-consistently supportive of Nb_2O_{5-x}'s outstanding high-rate performance in conjunction with facile electron and ion transport.

To further verify the above observations, we use a semi-empirical analysis to analyze the rate data from both the CV tests and the CC tests. In this analysis, we plot the data in Figure S13 against the scan rate v consistent with the following relation:

$$I = av^b$$

Alternatively, we also plot the data against cycle time (Figure 5C) to be compared with the following relation (Lin et al., 2015):

$$I = k_1v + k_2v^{1/2} \text{ or } I/v = k_1 + k_2v^{-1/2}$$

We obtain, for Nb_2O_{5-x}, b~0.9 (Figures S13A and S13B) throughout the voltage range (1–2 V), and k_1 = 349 F g^{-1} in Figure 5C in both the CV and CC tests. For diffusion-limited charge/discharge, b should be 0.5; for instantaneous, linear-capacitor-like charge/discharge, b should be 1.0, which is closer to the

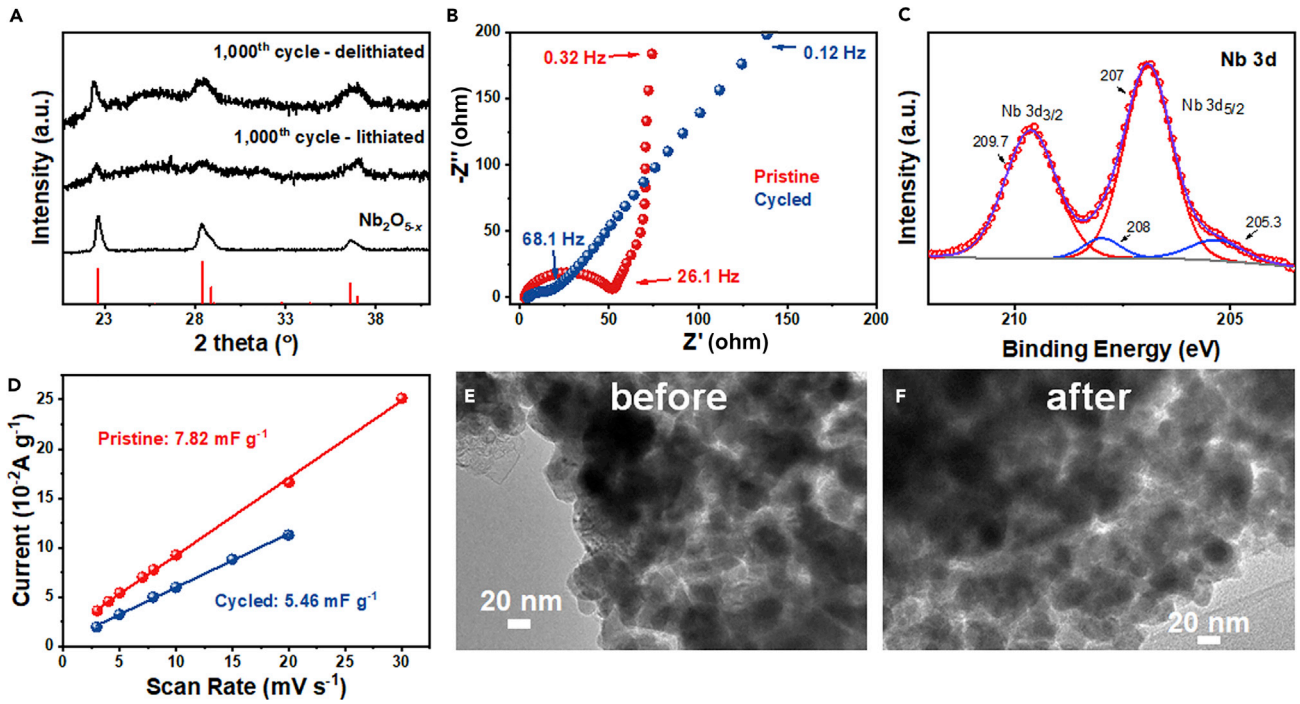

Figure 6. Changes after Long Cycles

(A–F) (A) XRD patterns of as-prepared Nb_2O_{5-x}, Li-charged (1 V) and Li-extracted (3 V) Nb_2O_{5-x} after 1,000 cycles; (B) Nyquist plots of pristine and cycled Nb_2O_{5-x}; (C) XPS spectra of cycled Li-extracted (3 V) Nb_2O_{5-x}, with best fit for Nb(V) in red and Nb(IV) in blue; (D) current as a function of scan rates for pristine and cycled Nb_2O_{5-x}, its slope providing C_L, and TEM images of Nb_2O_{5-x} electrode (E) before and (F) after 1000 cycles. (TEM samples prepared from powders scrapped off from the electrode.)

case here. Correspondingly, for rate-independent charge/discharge, k_1 should account for the entire specific capacitance, overwhelming the diffusion-dependent contribution of the $k_2 v^{-1/2}$ term, which is again close to the case here. In comparison, for Nb_2O_5, while b is still comparable or slightly smaller than that for Nb_2O_{5-x} (Figure S13), its $k_1 = 214$ F g^{-1} is considerably lower, indicating instantaneous linear-capacitor-like charge/discharge only makes a much smaller contribution. Specifically, we obtained the capacitor-like contribution of 58% for Nb_2O_5 compared with 87% for Nb_2O_{5-x}, which is extraordinarily high considering the fact that the well-celebrated pseudocapacitor, nanoparticle anatase TiO_2 (Wang et al., 2007), features only 55% according to our experience (see Figure S14.)

Therefore, a consistent picture emerges for Nb_2O_{5-x} as an excellent electrode with unusually fast charging/discharging kinetics, thanks to very fast ion and electron transport and very plentiful electrochemically active sites. To put these results into perspective, we compare the rate performance of Nb_2O_{5-x} with some Nb_2O_5-composite and two high-rate anode materials ($Li_4Ti_5O_{12}$ and TiO_2) in Figure 5D; outperformance of Nb_2O_{5-x} is apparent. Compared with other commercial common anode materials, our electrode has a higher capacity at high rates (213 and 204 mA h g^{-1} at 5 C and 10 C, respectively) outperforming graphite, Si/C, and $Li_4Ti_5O_{12}$ in Figures 5E and 5F. Although rate properties may be improved with delicate structural designs, as illustrated in hierarchical graphite wrapped Si—500 mA h g^{-1} at 5 C (Xu et al., 2017)—or by adding carbonaceous nano inclusions, e.g., in graphene-coated graphite—164 mA h g^{-1} at 5 C (Liu et al., 2016b)—these materials will have higher costs and lower tap densities, which adversely affects their practicality. In contrast, our Nb_2O_{5-x} is carbon free, has a reasonable tap density of 1.3 g cm^{-3}, allows volumetric capacity of up to 328, 243, 169, and 91 mA h cm^{-3} at 0.5 C, 25 C, 100 C, and 250 C, respectively, to be achieved and has been mass-produced (we achieved kg level production), which all bode well for making it a promising practical anode material.

Mechanism Investigation

Lastly, to confirm the excellent endurance of Nb_2O_{5-x} anodes, we examined the Li-charged and the Li-extracted states after 1,000 cycles and compared them with those of pristine Nb_2O_{5-x} before cycling.

Comparing their XRD (Figure 6A), we see despite peak broadening, crystallinity was maintained after cycling, indicating these sub-100 nm nanoparticles are structurally robust enough to withstand repeated Li-charging and extraction. Comparing their EIS (Figure 6B), although it has a lower slope closer to 45° at the low-to-intermediate frequency range after cycling, which is consistent with a more distributed resistive and capacitive character—perhaps caused by an increased frequency-dispersive conductivity (such as ion conductivity)—we see the charge transfer resistance is actually decreased by cycling. Comparing their Nb-3*d* XPS (Figure 6C *vs.* Figure S6A), we see cycling caused a significant increase of Nb (IV) compared with that in pristine Nb_2O_{5-x} (Figure S6A). Cycling, however, did cause a decrease in the equivalent specific capacitance C_L (Figure 6D, constructed from the CV data in Figures S10B and S10C), which is perhaps indicative of a decrease in the electrochemically active area because the charge transfer resistance did not suffer from cycling. On the other hand, these results could also be consistent with Li trapping at the active sites in Nb_2O_{5-x} after insertion, which leads to internal strains (thus broadening of XRD), loss of active sites (hence a smaller C_L), reduction of Nb (leaving Nb(IV)), and metal/ion conductivity (hence lower transfer resistance and battery-like charge storage EIS: in Figure 6B, pristine one from 26.1 Hz to 0.32 Hz; cycled one from 68.1 Hz to 0.12 Hz.). Of course, eventually, Li loss will deteriorate the Nb_2O_{5-x} electrode, which we did observe in past 4,000 cycles. Nevertheless, after 1,000 cycles, there was hardly any change in the microstructure according to TEM images (Figures 6E and 6F), attesting to the superior structural stability Nb_2O_{5-x}.

DISCUSSION

1. We have demonstrated that carbon-free defect-rich orthorhombic Nb_2O_{5-x} is an outstanding high-rate and durable LIBs' negative electrode material, having an excellent capacity of 253 mA h g^{-1} at 0.5 C, 187 mA h g^{-1} at 25 C of which 93% is retained after 4,000 cycles, and 130 mA h g^{-1} even at 100 C, much better than the commercial high-rate anode $Li_4Ti_5O_{12}$. Electrochemical kinetic analysis reveals that the energy storage is largely capacitive and non-solid-diffusion-limited in nature in this electrode.

2. A chemical processing strategy based on selective etching has been developed to maintain the crystal size and morphology of precursor powders but systematically reconstitute their unit cell composition into one appropriate for the final orthorhombic Nb_2O_{5-x}. The huge strain involved in reconstitution is instrumental to the preservation of the high defect density that is critical for the uncommon electrochemical activity.

3. The above finding and strategy may be applicable to other forms of Nb_2O_{5-x} and other oxides to enable high-performance new electrode materials. The simplicity and scalability of the fabrication method may allow large-scale industrial production.

Limitations of the Study

Although select etching as a synthesis method can be readily extended to many materials other than Nb_2O_5, it may be difficult to practice in doped materials if the dopant has a different chemistry from the main species. Etching is also likely to be sensitive to the surface structure, so the morphology of starting crystals could be critical. Future work is needed to define the universe of material composition and morphology suitable for this method.

METHODS

All methods can be found in the accompanying Transparent Methods supplemental file.

SUPPLEMENTAL INFORMATION

Supplemental Information can be found online at https://doi.org/10.1016/j.isci.2019.100767.

ACKNOWLEDGMENTS

This work was financially supported by National key R&D Program of China (Grant 2016YFB0901600), National Science Foundation of China (Grants No. 21871008 and 51672301), Science and Technology Commission of Shanghai (Grant 16JC1401700), and the Key Research Program of Chinese Academy of Sciences (Grant No. QYZDJ-SSW-JSC013).

AUTHOR CONTRIBUTIONS

Z.L. and W.D. performed the experiments and analyzed the data. J.W. contributed to optimizing synthesis condition of Nb_2O_{5-x}. C.D. and Y.L. carried out TEM imaging. Z.L. wrote the manuscript with contributions from all authors. I.W.C. and F.H. supervised the project and revised the manuscript.

DECLARATION OF INTERESTS

The authors declare no competing interests.

Received: July 9, 2019
Revised: October 26, 2019
Accepted: December 9, 2019
Published: January 24, 2020

REFERENCES

Augustyn, V., Come, J., Lowe, M.A., Kim, J.W., Taberna, P.-L., Tolbert, S.H., Abruña, H.D., Simon, P., and Dunn, B. (2013). High-rate electrochemical energy storage through Li^+ intercalation pseudocapacitance. Nat. Mater. *12*, 518–522.

Brezesinski, T., Wang, J., Tolbert, S.H., and Dunn, B. (2010). Ordered mesoporous alpha-MoO_3 with iso-oriented nanocrystalline walls for thin-film pseudocapacitors. Nat. Mater. *9*, 146–151.

Chen, X., Liu, L., Yu, P.Y., and Mao, S.S. (2011). Increasing solar absorption for photocatalysis with black hydrogenateed titanium dioxide nanocrystals. Science *331*, 5.

Chen, X., Liu, L., and Huang, F. (2015). Black titanium dioxide (TiO_2) nanomaterials. Chem. Soc. Rev. *44*, 1861–1885.

Come, J., Augustyn, V., Kim, J.W., Rozier, P., Taberna, P.-L., Gogotsi, P., Long, J.W., Dunn, B., and Simon, P. (2014). Electrochemical kinetics of nanostructured Nb_2O_5 electrodes. J. Electrochem. Soc. *161*, A718–A725.

Cui, H., Zhao, W., Yang, C., Yin, H., Lin, T., Shan, Y., Xie, Y., Gu, H., and Huang, F. (2014). Black TiO_2 nanotube arrays for high-efficiency photoelectrochemical water-splitting. J. Mater. Chem. A *2*, 8612–8616.

Deng, B., Lei, T., Zhu, W., Xiao, L., and Liu, J. (2018a). In-plane assembled orthorhombic Nb_2O_5 nanorod films with high-rate Li^+ intercalation for high-performance flexible Li-ion capacitors. Adv. Funct. Mater. *28*, 1704330.

Deng, Q., Li, M., Wang, J., Jiang, K., Hu, Z., and Chu, J. (2018b). Free-anchored Nb_2O_5@ graphene networks for ultrafast-stable lithium storage. Nanotechnology *29*, 185401.

Du, X., He, W., Zhang, X., Yue, Y., Liu, H., Zhang, X., Min, D., Ge, X., and Du, Y. (2012). Enhancing the electrochemical performance of lithium ion batteries using mesoporous $Li_3V_2(PO_4)_3$/C microspheres. J. Mater. Chem. *22*, 5960–5969.

Griffith, K.J., Forse, A.C., Griffin, J.M., and Grey, C.P. (2016). High-rate intercalation without nanostructuring in metastable Nb_2O_5 bronze phases. J. Am. Chem. Soc. *138*, 8888–8899.

Griffith, K.J., Wiaderek, K.M., Cibin, G., Marbella, L.E., and Grey, C.P. (2018). Niobium tungsten oxides for high-rate lithium-ion energy storage. Nature *559*, 556–563.

Kanno, R., and Murayama, M. (2001). Lithium ionic conductor Thio-LISICON: the Li_2S-GeS_2-P_2S_5 system. J. Electrochem. Soc. *148*, A742–A746.

Kim, J.W., Augustyn, V., and Dunn, B. (2012). The effect of crystallinity on the rapid pseudocapacitive response of Nb_2O_5. Adv. Energy Mater. *2*, 141–148.

Kodama, R., Terada, Y., Nakai, I., Komaba, S., and Kumagai, N. (2006). Electrochemical and in situ XAFS-XRD investigation of Nb_2O_5 for rechargeable lithium batteries. J. Electrochem. Soc. *153*, A583–A588.

Kong, L., Zhang, C., Zhang, S., Wang, J., Cai, R., Lv, C., Qiao, W., Ling, L., and Long, D. (2014). High-power and high-energy asymmetric supercapacitors based on Li^+-intercalation into a T-Nb_2O_5/graphene pseudocapacitive electrode. J. Mater. Chem. A *2*, 17962–17970.

Kong, L., Zhang, C., Wang, J., Qiao, W., Ling, L., and Long, D. (2015). Free-standing T-Nb_2O_5/graphene composite papers with ultrahigh gravimetric/volumetric capacitance for Li-ion intercalation pseudocapacitor. ACS Nano *9*, 11200–11208.

Kumagai, N., Koishikawa, Y., Komaba, S., and Koshiba, N. (1999). Thermodynamics and kinetics of lithium intercalation into Nb_2O_5 electrodes for a 2V rechargeable lithium battery. J. Electrochem. Soc. *146*, 3203–3210.

Lin, T., Chen, I.W., Liu, F., Yang, C., Bi, H., Xu, F., and Huang, F. (2015). Nitrogen-doped mesoporous carbon of extraordinary capacitance for electrochemical energy storage. Science *350*, 1508–1513.

Liu, H., Bi, Z., Sun, X.G., Unocic, R.R., Paranthaman, M.P., Dai, S., and Brown, G.M. (2011). Mesoporous TiO_2–B microspheres with superior rate performance for lithium ion batteries. Adv. Mater. *23*, 3450–3454.

Liu, S., Zhou, J., Cai, Z., Fang, G., Pan, A., and Liang, S. (2016a). Nb_2O_5 microstructures: a high-performance anode for lithium ion batteries. Nanotechnology *27*, 46LT01.

Liu, X., Liu, E., Chao, D., Chen, L., Liu, S., Wang, J., Li, Y., Zhao, J., Kang, Y.-M., and Shen, Z. (2016b). Large size nitrogen-doped graphene-coated graphite for high performance lithium-ion battery anode. RSC Adv. *6*, 104010–104015.

Lubimtsev, A.A., Kent, P.R.C., Sumpter, B.G., and Ganesh, P. (2013). Understanding the origin of high-rate intercalation pseudocapacitance in Nb_2O_5 crystals. J. Mater. Chem. A *1*, 14951.

Song, M.Y., Kim, N.R., Yoon, H.J., Cho, S.Y., Jin, H.-J., and Yun, Y.S. (2017). Long-lasting Nb_2O_5-based nanocomposite materials for Li-ion storage. ACS Appl. Mater. Interfaces *9*, 2267–2274.

Sun, H., Mei, L., Liang, J., Zhao, Z., Lee, C., Fei, H., Ding, M., Lau, J., Li, M., and Wang, C. (2017). Three-dimensional holey-graphene/niobia composite architectures for ultrahigh-rate energy storage. Science *356*, 599–604.

Viet, A.L., Reddy, M.V., Jose, R., Chowdari, B.V.R., and Ramakrishna, S. (2010). Nanostructured Nb_2O_5 polymorphs by electrospinning for rechargeable lithium batteries. J. Phys. Chem. C *114*, 664–671.

Wang, J., Polleux, J., Lim, J., and Dunn, B. (2007). Pseudocapacitive contributions to electrochemical energy storage in TiO_2 (anatase) nanoparticles. J. Phys. Chem. C *111*, 14925–14931.

Wang, G., Wang, H., Ling, Y., Tang, Y., Yang, X., Fitzmorris, R.C., Wang, C., Zhang, J.Z., and Li, Y. (2011). Hydrogen-treated TiO_2 nanowire arrays for photoelectrochemical water splitting. Nano Lett. *11*, 3026–3033.

Wang, Z., Yang, C., Lin, T., Yin, H., Chen, P., Wan, D., Xu, F., Huang, F., Lin, J., Xie, X., et al. (2013a). H-doped black titania with very high solar absorption and excellent photocatalysis enhanced by localized surface plasmon resonance. Adv. Funct. Mater. *23*, 5444–5450.

Wang, Z., Yang, C., Lin, T., Yin, H., Chen, P., Wan, D., Xu, F., Huang, F., Lin, J., Xie, X., et al. (2013b). Visible-light photocatalytic, solar thermal and photoelectrochemical properties of aluminium-reduced black titania. Energ. Environ. Sci. *6*, 3007–3014.

Wang, C., Wang, S., He, Y.-B., Tang, L., Han, C., Yang, C., Wagemaker, M., Li, B., Yang, Q.-H., and Kim, J.-K. (2015). Combining fast Li-ion battery cycling with large volumetric energy density: grain boundary induced high electronic and ionic conductivity in $Li_4Ti_5O_{12}$ spheres of densely packed nanocrystallites. Chem. Mater. *27*, 5647–5656.

Wei, M., Wei, K., Ichihara, M., and Zhou, H. (2008). Nb_2O_5 nanobelts: a lithium intercalation host with large capacity and high rate capability. Electrochem. Commun. *10*, 980–983.

Xie, J., Zhang, X., Zhang, H., Zhang, J., Li, S., Wang, R., Pan, B., and Xie, Y. (2017). Intralayered Ostwald ripening to ultrathin nanomesh catalyst with robust oxygen-evolving performance. Adv. Mater. *29*, 1604765.

Xu, Q., Li, J.Y., Sun, J.K., Yin, Y.X., Wan, L.J., and Guo, Y.G. (2017). Watermelon-inspired Si/C microspheres with hierarchical buffer structures for densely compacted lithium-ion battery anodes. Adv. Energy Mater. *7*, 1601481.

ISCI, Volume *23*

Supplemental Information

Orthorhombic Nb_2O_{5-x} for Durable High-Rate Anode of Li-Ion Batteries

Zichao Liu, Wujie Dong, Jianbo Wang, Chenlong Dong, Yue Lin, I-Wei Chen, and Fuqiang Huang

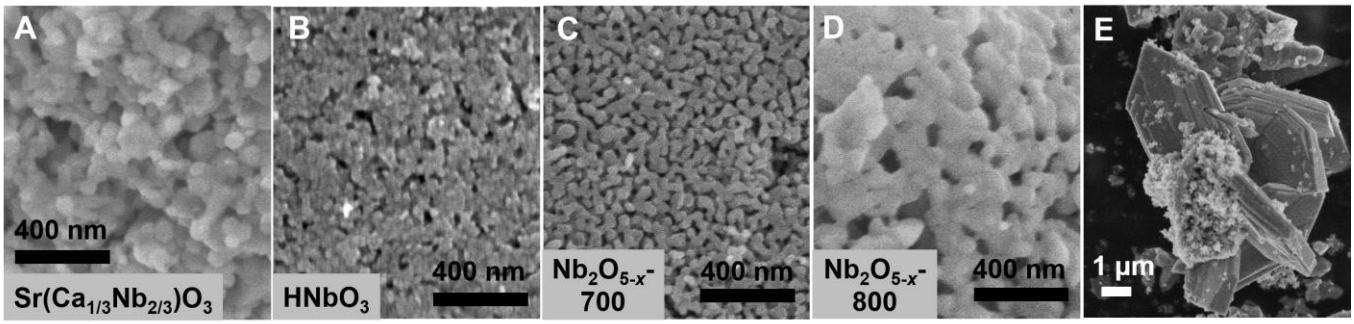

Fig. S1. SEM images. Related to Fig. 1. (**A**) $Sr(Ca_{1/3}Nb_{2/3})O_3$, (**B**) $HNbO_3$, (**C**) 700 °C annealed Nb_2O_{5-x}, (**D**) 800 °C annealed Nb_2O_{5-x}, and (**E**) dissolved-and-recrystallized $HNbO_3$. (**A-C**) have similar characteristic length scale.

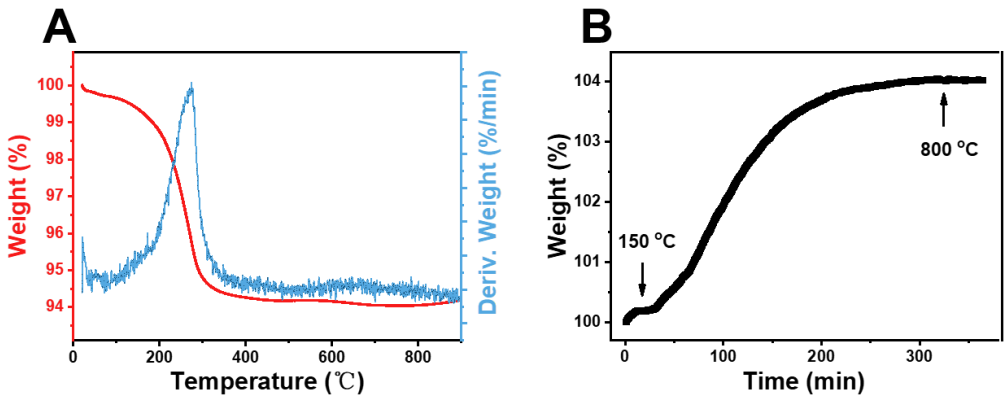

Fig. S2. Thermogravimetric analysis data. Related to Fig. 2. (**A**) $HNbO_3$ in N_2 atmosphere showing ~6% weight loss due to dehydration, and (**B**) Nb_2O_{5-x} in air showing ~4% weight gain due to re-oxidation. From (**B**), we calculated x=0.61.

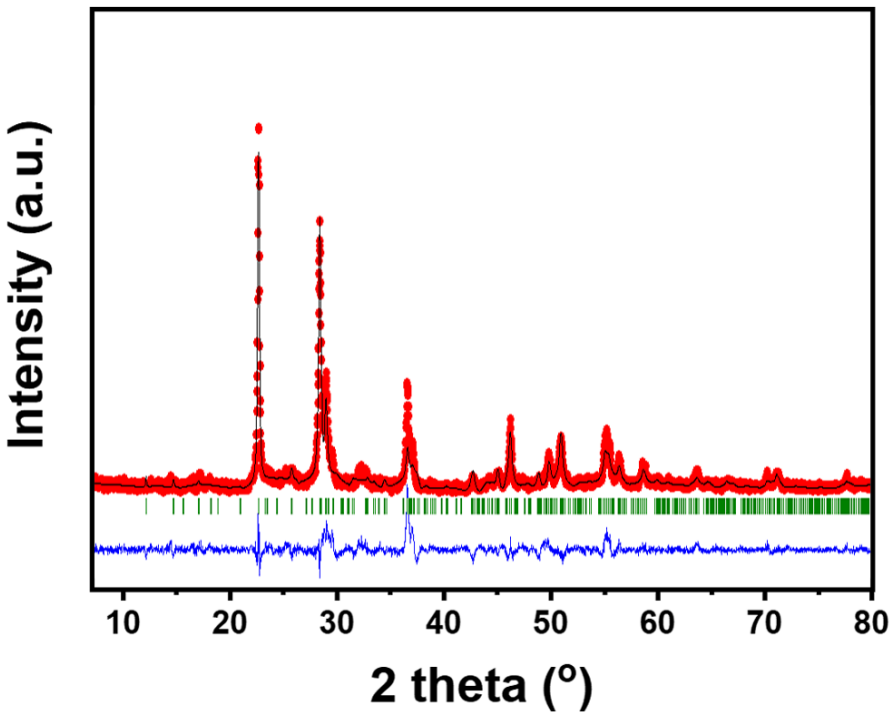

Fig. S3. Rietveld refinement of the powder XRD pattern of Nb_2O_{5-x}. Related to Fig. 2. Observed (circles) and calculated (continuous line) profiles of Nb_2O_{5-x} using space group Pbma. Tick marks below indicate positions of allowed Bragg's reflections. A difference curve ($I_{obs.} - I_{calc.}$) is shown at bottom. The structure refinement was stable and converged rapidly with Chi squared χ^2=2.89, R-factor=14.8.

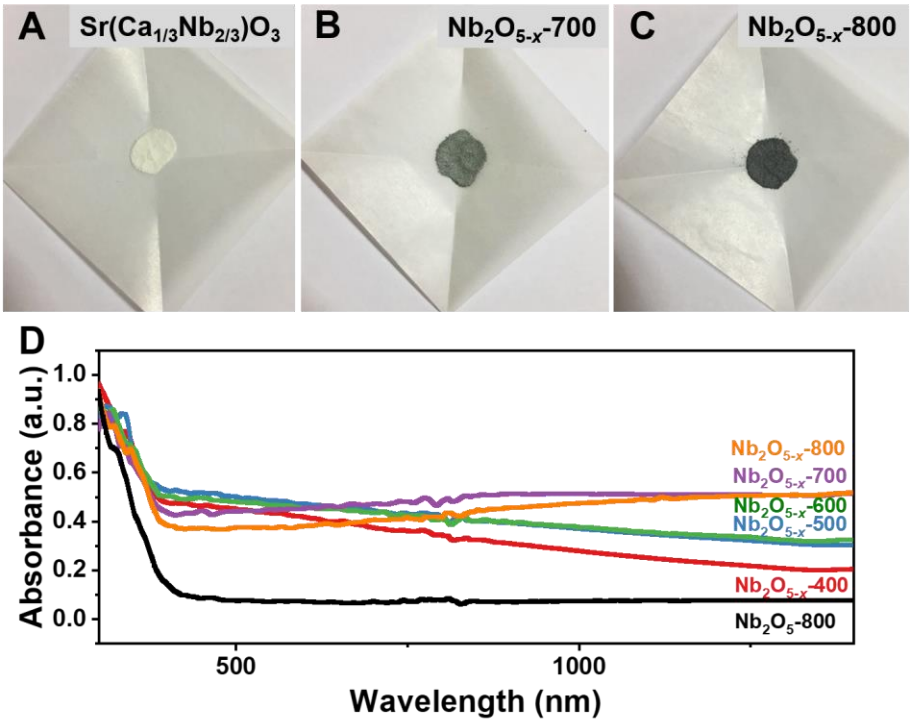

Fig. S4. Optical images and UV-vis diffuse reflectance spectra. Related to Fig. 2. Optical images of (**A**) complex oxide precursor $Sr(Ca_{1/3}Nb_{2/3})O_3$, (**B**) 700 °C-Ar-annealed Nb_2O_{5-x}, (**C**) 800 °C-Ar-annealed Nb_2O_{5-x}. (**D**) UV-vis diffuse reflectance spectra of sample annealed in Ar from 400 °C to 800 °C and in air at 800 °C (black line).

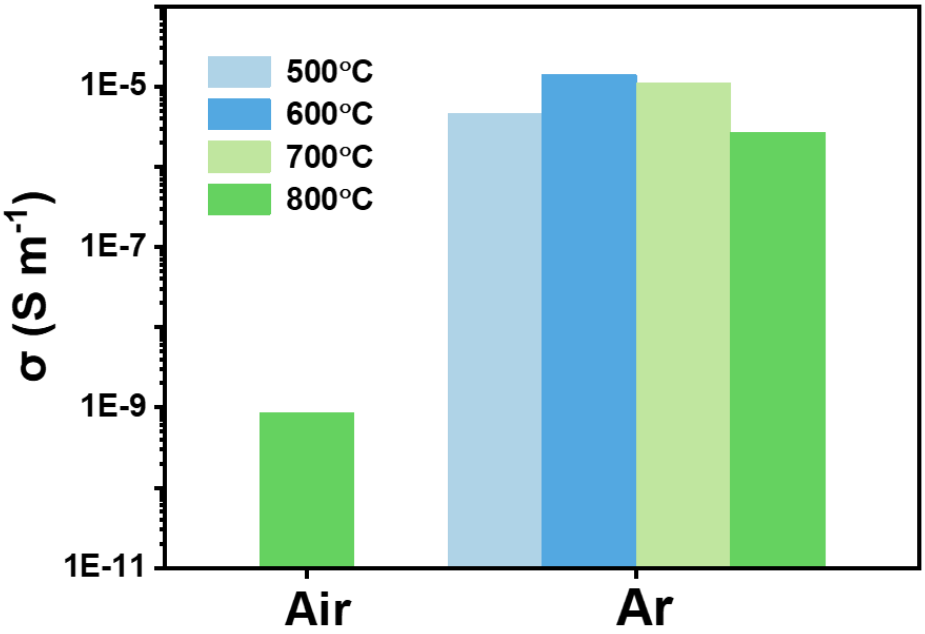

Fig. S5. Conductivity of products in different annealing conditions. Related to Fig. 2.
500 °C-, 600 °C-, 700 °C-, 800 °C-Ar annealed Nb_2O_{5-x}, plus 800 °C-air annealed Nb_2O_5.

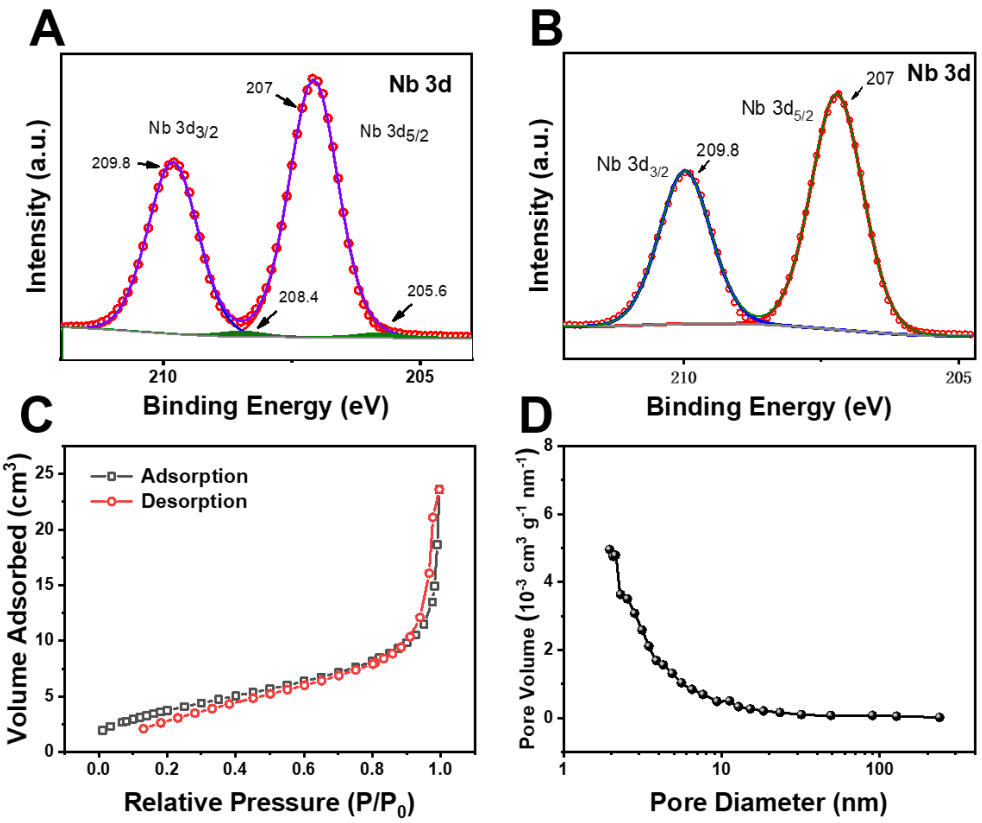

Fig. S6. XPS data with specific surface area and pore size distribution analysis. Related to Fig. 2. XPS spectra of (**A**) black Nb_2O_{5-x}, and (**B**) white Nb_2O_5. (**C**) Nitrogen adsorption-desorption isotherms and (**D**) BJH adsorption pore size distribution analysis for Nb_2O_{5-x}.

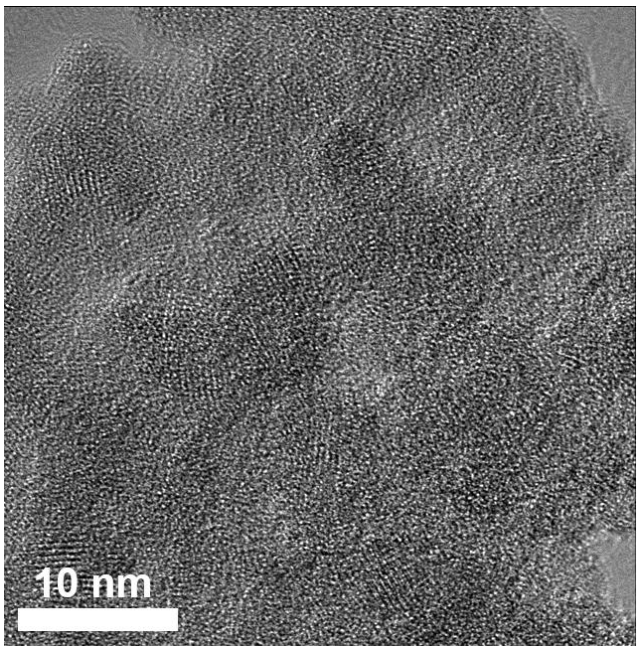

Fig. S7. TEM image of $HNbO_3$. Related to Fig. 3. Crystallites are about 5 nm in size, some apparently highly disordered.

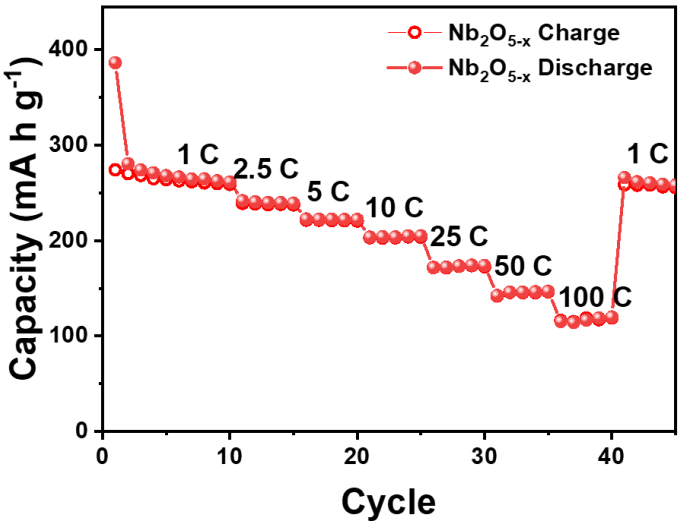

Fig. S8. Related to Fig. 4. Rate performance of Nb_2O_{5-x} with Al foil as current collector.

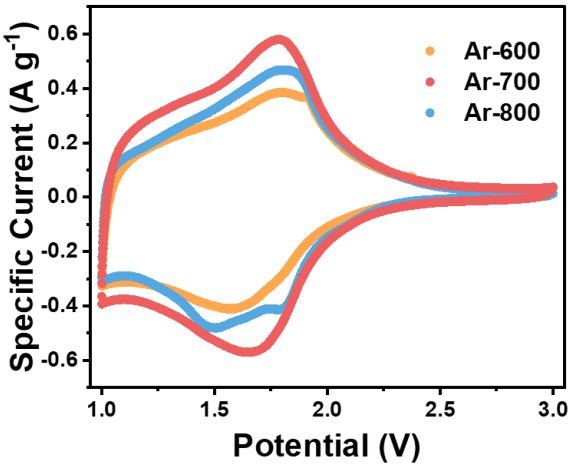

Fig. S9. CV curves of Nb_2O_{5-x} annealed at different temperatures. Related to Fig. 5. The result identifies optimal annealing condition is 700 °C.

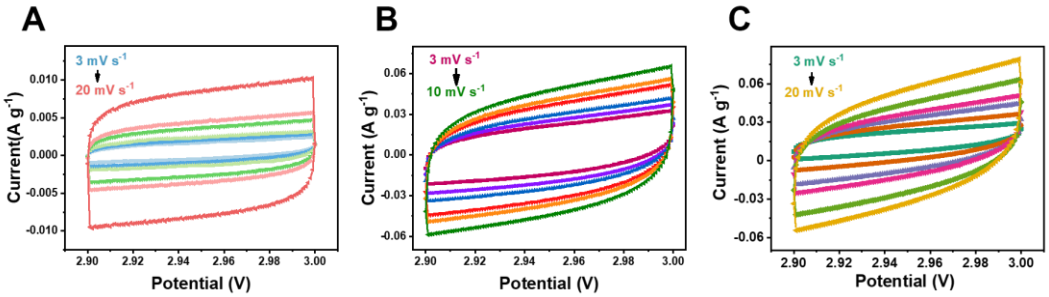

Fig. S10. CVs which equivalent specific capacitance is constructed from. Related to Fig. 5. CVs of (**A**) Nb_2O_5, (**B**) pristine and (**C**) 1,000-cycled Nb_2O_{5-x} at scan rates from 3 to 20 mV s^{-1} over 2.9 - 3 V.

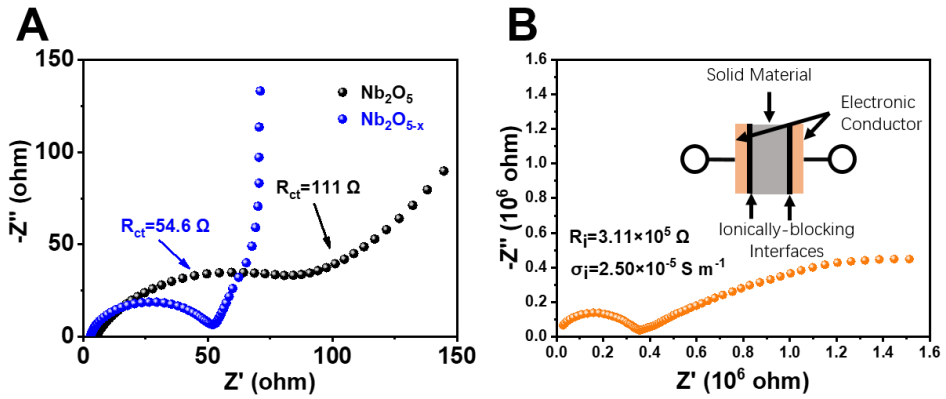

Fig. S11. Nyquist plots of Nb_2O_5, Nb_2O_{5-x} electrodes and Nb_2O_{5-x} pellet. Related to Fig. 5. Nyquist plots to evaluate (**A**) charge transfer resistance of Nb_2O_{5-x} and Nb_2O_5 electrodes and (**B**) ionic conductivity at room temperature of pressed Nb_2O_{5-x} pellet. (Inset: schematic experimental setup for (**B**).)

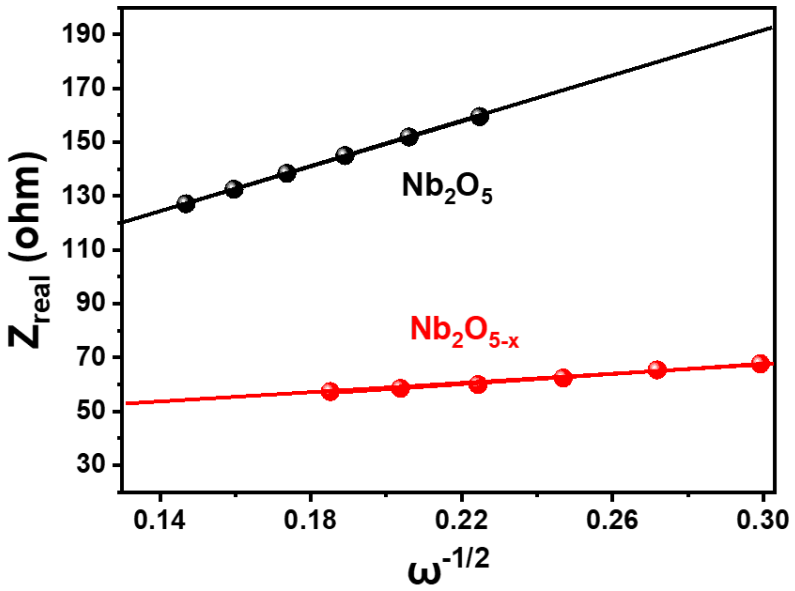

Fig. S12. Linear fitting of Z_{real} *vs.* $\omega^{-1/2}$. Related to Fig. 5. Warburg plot of real part of impedance *vs*. inverse square root of ω in the low-frequency region, from which the slope σ can be obtained.

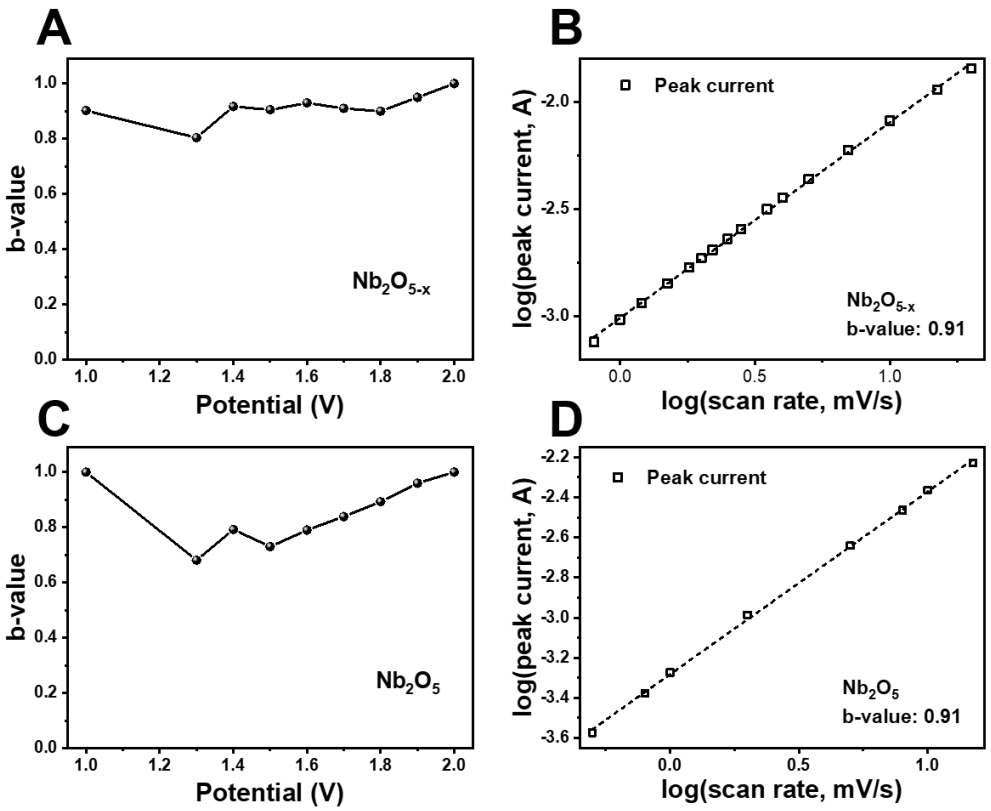

Fig. S13. *b*-values analysis. Related to Fig. 5. (**A**) *b*-values of Nb_2O_{5-x} determined from (**B**) plot of current *vs*. potential; likewise, (**C**) *b*-values of Nb_2O_5 determined from (**D**) plot of current *vs*. potential.

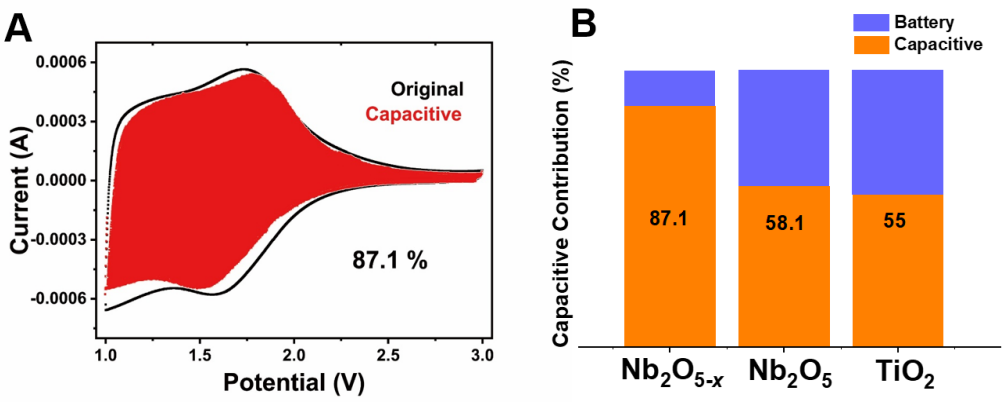

Fig. S14. Contribution and percentage of capacitive contribution. Related to Fig. 5. (**A**) Capacitor-like contribution in the total capacity of Nb_2O_{5-x}. (**B**) Percentages of capacitive contributions in Nb_2O_{5-x}, Nb_2O_5 and TiO_2 (anatase).

Transparent Methods

Preparation of $Sr(Ca_{1/3}Nb_{2/3})O_3$, Nb_2O_5, $HNbO_3$ and Nb_2O_{5-x}

The parent oxide to be used for selective acid etching was $Sr(Ca_{1/3}Nb_{2/3})O_3$. It was synthesized by a sol-gel method starting with a solution of $SrCl_2{\cdot}6H_2O$ (0.74 g), $CaCl_2$ (0.1027 g) and citric acid monohydrate (3.5 g) in 7.5 mL deionized water, to which 7.5 mL ethylene glycol was added to stabilize the solution. A second solution of 0.5 g $NbCl_5$ in 15 mL ethyl alcohol was next added to the first, and the mixture was heated to 90 °C and held there until it gelled. The transparent yellow gel was calcined at 700 °C in air for 3 h to obtain $Sr(Ca_{1/3}Nb_{2/3})O_3$ powders. Similarly, Nb_2O_5 was synthesized using the same procedure but without $SrCl_2$ and $CaCl_2$.

Powder of $Sr(Ca_{1/3}Nb_{2/3})O_3$ was used to prepare $HNbO_3$ via acid etching, in which 13 mL 0.5 M HCl with 0.2 g $Sr(Ca_{1/3}Nb_{2/3})O_3$ addition was left in a 25 mL Teflon-lined steel autoclave at 200 °C for 12 h. The etched powders were washed several times with deionized water and dried at 70 °C to obtain $HNbO_3$. Finally, Nb_2O_{5-x} was obtained by annealing $HNbO_3$ at 700 °C for 4 h in an Ar atmosphere. A schematic summarizing the above is shown in Fig. 1.

Characterization of materials

The crystal structures of as-prepared materials were determined by X-ray diffraction (XRD, Bruker D2 phaser diffractometer, 4 kW) using Cu *K*α radiation (λ = 0.15406 nm). Their morphology and microstructure were observed using a scanning electron microscope (SEM, Phenom Pro) and a transmission electron microscope (TEM, JEM2010-HR). Nitrogen adsorption/desorption isotherms at 77 K were collected by a Micrometrics ASAP 2010 analyzer, and analyzed by the Brunauer-Emmett-Teller (BET) method for the specific surface area and the Barrett-Joyner-Halenda (BJH) model for the pore size distribution. Thermal decomposition of $HNbO_3$ was studied using a thermal gravimetric analyzer (Thermal Analysis Q600SDT) at a heating rate of 10 °C min^{-1} from room temperature to 900 °C. X-ray photoelectron spectroscopy (XPS) was carried out on a RBD upgraded PHI-5000C ESCA system (Perkin Elmer) with Mg *K*α radiation (*hv* = 1253.6 eV), and electron paramagnetic resonance (EPR) spectra were collected using a Bruker EMX-8 spectrometer at 9.44 GHz at 300 K. Magnetic and electrical properties were also studied in a Physical Property Measurement System (PPMS, Quantum Design). UV-Vis diffuse reflectance spectra were performed at room temperature using a UV-4100 spectrophotometer operating from 1400 nm to 300nm. $BaSO_4$ was used as a 100 % reflectance standard. The powder sample was spread on a compacted base of $BaSO_4$ powder. The tap density was measured by mechanically tapping a 2-mL graduated cylinder, which contained the sample powder, until no more volume change was observed. The tap density was obtained by dividing powder mass by the final volume of the tapped powder.

Electrochemical characterizations

Electrochemical performance was evaluated using CR2016 coin cells with Nb_2O_{5-x} and Nb_2O_5 anodes assembled in an Ar-filled glove box. The slurry for the electrode was made of

80 wt% active material (Nb_2O_{5-x} or Nb_2O_5), 10 wt% conductive agent (acetylene black) and 10 wt% polyvinylidene fluoride (PVDF), the latter dissolved in N-methyl-2-pyrrolidone (NMP) before use. The slurry was cast onto a copper foil and dried at 70 °C for 7 h. The cell was then assembled using a pure Li foil as the counter electrode, a microporous polypropylene film (Whatman, GF/C) as the separator, and a mixture of ethylene carbonate, diethylene carbonate and dimethyl carbonate (1:1:1 in weight) with 1M $LiPF_6$ as electrolyte. For comparison (in Fig. 5E-F) commercial anode materials (Si/C and graphite purchased from BTR, P. R. China and MTI, P. R. China, respectively) were also assembled into coin cells using the same process. Galvanostatic charge-discharge (CC) tests and cyclic voltammetry (CV) were conducted between 1.0 and 3.0 V *vs.* Li/Li^+ at room temperature in a LAND battery testing system. Lastly, electrochemical impedance spectroscopy (EIS) was measured using a CHI760E electrochemical workstation (Chenhua instrument, Shanghai, China).

The EIS data in the Nyquist plots have a semicircle in the high frequency range that indicates the charge transfer resistance, and an inclined line in the low frequency range that indicates Li^+ diffusion into the bulk of the electrode; the latter commonly referred to as Warburg diffusion. The diffusion coefficient of Li^+ can be calculated from the latter part using the following equation:

$$D_{Li^+} = 0.5 \times \left[\frac{V_m}{FS\sigma}\left(-\frac{dE}{dx}\right)\right]^2$$

Here, V_m is the molecular volume ($cm^3\ mol^{-1}$), S is the electrode area (cm^2), $\frac{dE}{dx}$ is the slope of the Coulometric titration plot, F is the Faraday constant (96, 486 C mol^{-1}), and σ is the Warburg factor which can be obtained from the EIS using the following relationship:

$$Z_{real} = R_\Omega + R_{ct} + \sigma\omega^{-1/2}$$

with R_Ω being the resistance between the electrolyte and electrode, R_{ct} the charge transfer resistance, and ω the angle frequency. This leads to a linear dependence of Z_{real} *vs.* $\omega^{-1/2}$, shown in **Fig. S12** using our data, from which the slope σ can be obtained. An increased D_{Li+} implied faster Li^+ transport and electrochemical kinetics.